Journal of Molecular Liquids 309 (2020) 113066

Contents lists available at ScienceDirect

Journal of Molecular Liquids

journal homepage: www.elsevier.com/locate/molliq

A colloid approach to decorate latex particles with Prussian blue nanozymes

Nizar B. Alsharif [a], Gergely F. Samu [b], Szilárd Sáringer [a,b], Szabolcs Muráth [a,b], Istvan Szilagyi [a,b,*]

[a] MTA-SZTE Lendület Biocolloids Research Group, University of Szeged, H-6720 Szeged, Hungary
[b] Interdisciplinary Excellence Center, Department of Physical Chemistry and Materials Science, University of Szeged, H-6720 Szeged, Hungary

ARTICLE INFO

Article history:
Received 25 February 2020
Received in revised form 30 March 2020
Accepted 1 April 2020
Available online 18 April 2020

Keywords:
Heteroaggregation
Enzyme mimic
Prussian blue
Latex
Colloidal stability

ABSTRACT

Prussian blue (PB) nanoparticles of intrinsic peroxidase and superoxide dismutase-like activities were prepared by the co-precipitation method and immobilized on amidine functionalized polystyrene latex (AL) particles. The interaction between the AL and PB particles and the colloidal stability of the resulting AL-PB hybrid composites were assessed at different mass ratios via determination of the charging and aggregation characteristics in the samples. The negatively charged PB nanoparticles strongly adsorbed on the oppositely charged AL particles resulting in a range of AL-PB composites of positive, neutral and negative overall charge, once the PB dose was increased. The AL-PB composite of a saturated PB layer on the surface of the AL particles formed considerably stable dispersions. Further, the morphology, structural and functional features of the AL-PB composites were explored by electron microscopy and enzymatic assays. The results revealed that the immobilization of PB nanoparticles not only provided a sustained catalytic surface but did not compromise the enzyme-like activities. The obtained stable composite is a promising agent in antioxidant therapies and wherever the aim is to reduce oxidative stress at laboratory or larger scales.

1. Introduction

Although natural enzymes are remarkable catalysts under designated conditions, their production and purification is expensive and time-consuming [1]. More importantly, they suffer from inherent instability leading to a narrow window of operational conditions such as pH, pressure or temperature [2]. Under harsh conditions, protein structures denature, which causes a permanent loss of catalytic activity. Such drawbacks prompted the need for artificial enzymes, which are stable and low-cost materials possessing catalytic potential of the corresponding natural enzyme. Nanomaterials of enzymatic function (so-called nanozymes) have been heavily explored as alternatives for native proteins due to their large surface area, high reactivity and tunable physico-chemical properties [3]. These nanozymes comprise a vast variety of nanostructures and enzymatic activities [4–6].

Among them are nanozymes of antioxidant properties, which represent an important class of materials used for decomposition of reactive oxygen species (ROS) [7], whose presence gives rise to the evolution of various diseases in living organisms [8,9] and to lower quality products in industrial processes [10,11]. Accordingly, various nanoparticles have been prepared and proved as efficient ROS scavenging catalysts, those include vanadium-pentoxide [12], copper [13], gold [14], platinum [15], molybdenum-disulfide [16], manganese oxide [17], cerium-oxide [18], carbonaceous [19], iron-cyanide [20] and hybrid [21] particles.

Prussian blue (PB), a mixed valence iron-cyanide complex, is a multifunctional material in both pure and composite forms. Apart from the utilization in ROS decomposition, PB was also used as a biomarker [22], a biomedical therapeutic agent [23] and a key part of electrochemical sensors [24]. Due to their low long-term toxicity [25] and that their presence in cells does not trigger production of hydroxyl radicals [26], application of PB nanostructures has attracted significant contemporary interest in the scientific community. They act as efficient functional mimic of superoxide dismutase (SOD), catalase and peroxidase enzymes due to their high affinity to oxygen-bearing radicals [20]. For instance, polymer-PB composites were prepared at different polymer molecular weights, whose optimal value had to be determined to obtain the most efficient ROS-scavenging activity in cells under stimulated oxidative stress [27]. A magnetic composite, which consists of iron-oxide core and PB shell was prepared and showed excellent peroxidase-like activity, i.e., H_2O_2-consuming ability, in laboratory test reactions [28]. Cubic PB nanoparticles were prepared in a polymer-assisted synthetic process and they sufficiently mimicked the function of a number of antioxidant enzymes under cellular environment [20]. Kinetic analysis of the test reactions revealed that such a multi-enzymatic activity

* Corresponding author at: MTA-SZTE Lendület Biocolloids Research Group, University of Szeged, H-6720 Szeged, Hungary.
E-mail address: szistvan@chem.u-szeged.hu (I. Szilagyi).

https://doi.org/10.1016/j.molliq.2020.113066

originates from the abundant redox potentials due to the different forms of iron in the material.

The stability of PB systems plays a key role in determining the suitability for a potential utilization. In most of the applications, PB nanoparticles are dispersed in liquid medium such as blood and cellular cytoplasm in living organisms as well as in industrial liquors during manufacturing processes. The colloidal stability of such systems is of special importance, since particle aggregation may lead to significant loss of the catalytic activity. Thus, surface modification of PB nanoparticles was performed with poly(ethylene glycol) [29], poly(diallyldimethylammonium chloride) [30], chitosan [31], native proteins [28] and poly(vinylpyrrolidone) [32] macromolecules to improve their dispersibility. Nevertheless, there is a lack of comprehensive studies on charging and aggregation of polymer functionalized PB particles. A deep understanding of colloidal stability and the factors that adversely affect it, is extremely important to obtain viable and robust colloidal PB systems.

In the present work, PB nanoparticles were prepared and immobilized on amidine functionalized polystyrene latex particles via controlled heteroaggregation. Such a procedure improved the colloidal stability of the PB nanoparticles as well as bound them to AL surface to increase their local concentration. The experimental conditions were optimized by following the charging and aggregation processes in the samples with microscopy, spectrophotometry and light scattering techniques, while the antioxidant property of the as-prepared and immobilized PB nanoparticles was assessed by enzymatic assays.

2. Experimental and methods

2.1. Materials

H_2O_2 (30% m/m), HCl (37% m/m), KCl (≥99.5%), acetone (≥99.8%), $K_3[Fe(CN)_6]$ (≥99.0%) and phosphate buffer were purchased from VWR™. Guaiacol (99%) and $FeCl_2 \cdot 4H_2O$ (≥99%) were acquired from Acros Organics. Amidine latex beads (AL in 4% w/v dispersions) were purchased from Invitrogen™. The AL particles are positively charged at low pH due to the protonation of the surface functional groups. Surface charge density of AL is +19.7 μC/cm^2, the beads have a mean diameter of (0.51 ± 0.02) μm and a coefficient of size variation of 4.6%, as determined by the manufacturer with electron microscopy. Hellmanex® III cleaning agent was bought from Hellma. Xanthine (99%) was purchased from Alfa Aesar. Xanthine oxidase (lyophilized powder, 0.4–1.0 units/mg protein) was bought from Sigma-Aldrich. The pH was kept at (4.0 ± 0.2) throughout all experiments, except otherwise indicated. The VWR™ Puranity TU 3 UV/UF+ system was used to obtain ultrapure water, which was further filtered using PVDF-based 0.1 μm syringe filters purchased from MILLEX®VV.

2.2. Preparation of PB particles and AL-PB hybrids

The PB nanoparticles were synthesized by the co-precipitation method [33]. The glasswares were carefully cleaned with Hellmanex® III and concentrated HCl solution. Under vigorous stirring, a 1.0 mM aqueous solution of $K_3[Fe(CN)_6]$ (100 mL) was added dropwise to 100 mL of 1.0 mM $FeCl_2$. After that, 400 mL of acetone was added to the resultant dark blue mixture. The solid materials were collected by centrifugation at a rate of 9000 rpm for 30 min and cleaned with acetone. The centrifugation process was repeated till all the PB was collected. Finally, the obtained PB nanoparticles were dispersed in a certain amount of ultrapure water to obtain a 10 g/L stock.

The immobilization of PB nanoparticles on the surface of AL to form AL-PB composites was achieved by simple mixing of proper volumes of PB and AL stocks, followed by the addition of a calculated volume of KCl solution to fix the ionic strength in the samples. The origin of the driving forces was electrostatic due to the oppositely charged PB and AL particles under the experimental conditions applied. The final AL-PB dispersions were homogenized by ultrasonication for 1 h. The concentration of PB and AL particles in the composite dispersions was expressed as dose in milligrams of PB per one gram of AL (denoted as mg/g hereafter).

2.3. Electrophoretic light scattering

Electrophoretic mobility values were determined using an Anton Paar Litesizer™ 500 device equipped with a 658 nm wavelength laser source, with the applied voltage kept at 200 V throughout all electrophoretic light scattering measurements.

The pH-dependent surface charging of PB nanoparticles was studied with 100 ppm PB dispersions at different pH values. Concerning sample preparation, two 100 ppm stock PB dispersions were prepared and the pH was adjusted to 3 and 11, respectively. Then, a series of 8 mL PB dispersions was prepared by mixing different volumes of the two stocks, so that the pH in the series of dispersions gradually changed from 3 to 11. After each mixing, the resulting dispersion was homogenized by vortex and its pH value was unambiguously measured with a WTW pH benchtop meter (inoLab® pH 7310).

During the determination of the mobilities of the AL particles at different salt concentrations, a series of 25 ppm AL dispersions was prepared in the 1–1750 mM KCl concentration range. The effect of PB-to-AL mass ratio on the surface charge was determined in the 1–1000 mg/g PB dose regime at 1 mM ionic strength adjusted by addition of KCl. In each sample, the AL concentration was kept at 25 ppm, while the amount of PB particles was adjusted to the desired dose.

In general, the prepared dispersions were left to equilibrate for 2 h at room temperature. For the measurements, 350 μL samples were withdrawn from the dispersion of interest and were transferred to an omega cuvette (Anton Paar™). The electrophoretic mobility measurement was then performed at (25.0 ± 0.2) °C and reported as an average of 5 runs.

2.4. Dynamic light scattering

The hydrodynamic radius of the particles was determined by dynamic light scattering (DLS) using an ALV-NIBS/HPPS Particle sizer equipped with a 632.8 nm laser source. The scattered light was collected at 173° and data analysis was based on the cumulant fit [34].

The sample preparation protocols were identical to the ones described in the electrophoretic part above, with the exception that each measurement was started immediately after addition of the desired volume of AL or PB to the corresponding sample. The total volume of each sample was 2.0 mL and the experiments were carried out in disposable polystyrene cuvettes at (25.0 ± 0.2) °C.

In the time resolved setup, the hydrodynamic radius versus time curves contained 30–100 measurement points for each sample depending on the speed of the aggregation. The colloidal stability was expressed in terms of stability ratio (W), which was calculated using the following equation [34,35].

$$W = \frac{k_{app(fast)}}{k_{app}} \quad (1)$$

where k_{app} is the apparent aggregation rate constant and $k_{app(fast)}$ is the apparent aggregation rate constant in a dispersion containing 1.0 M KCl. Under this condition, the aggregation is controlled solely by the diffusion of the particles, i.e., rapid particle aggregation occurs. The apparent aggregation rate constant was calculated from the hydrodynamic radius (R_h) versus time (t) plots as follows.

$$k_{app} = \frac{1}{R_h(0)} \frac{dR_h(t)}{dt} \quad (2)$$

where $R_h(0)$ is the hydrodynamic radius of the monomer particles and $\frac{dR_h(t)}{dt}$ is the slope of the linear fit of the R_h versus t data points of the sample of interest. Note that stability ratios close to unity refer to

rapid or diffusion-controlled aggregation, while higher values indicate more stable samples.

2.5. Electron microscopy

The morphologies of the particles and their composites were analyzed by scanning (SEM, Hitachi S4700) and transmission electron microscopy (TEM, FEI Tecnai G2). Two 25 ppm dispersions of PB and AL as well as dispersions at PB doses of 1, 30 and 600 mg PB/g AL were imaged. For TEM, a volume of 5 μL of each sample was introduced onto a copper-coated carbon mesh. Each aliquot was allowed to adsorb for 10 s, before removing the drop and introducing the next one. The sample grids were prepared 30 min before the measurements. For SEM, 5 μL portions of all dispersions were introduced onto the SEM sample holder, a piece of silicon wafer on an aluminum disk. The samples were dried for a few minutes before being sputter coated with a thin gold film for 30 s. The sample holder was then introduced into the microscope for imaging.

2.6. X-ray photoelectron spectroscopy

The X-ray photoelectron spectroscopy (XPS) measurements were carried out with a SPECS™ instrument equipped with a PHOIBOS 150 MCD 9 hemispherical analyzer, under a main-chamber pressure in the 10^{-9}–10^{-10} mbar range. The analyzer was in fixed analyzer transmission mode with 40 eV pass energy for the survey scan and 20 eV pass energy for the high-resolution scans. The PB sample powder was pressed into an indium foil and loaded into the chamber on a gold-coated sample holder. Al Kα X-ray source was used at 14 kV and at 150 W power. Charge referencing was done to the adventitious carbon (284.8 eV) on the surface of the sample. For spectrum evaluation, CasaXPS commercial software package was used.

2.7. UV–Vis spectrophotometry

The UV–Vis spectra were recorded with a GENESYS™ 10S UV–Vis spectrophotometer (Thermo Scientific) in the wavelength range of 300–900 nm. For PB analysis, 100 ppm dispersion was prepared in ultrapure water. The blank cuvette was filled with filtered water. After the sample was homogenized by ultrasonication for 10 min, the spectrum was recorded at a scan step of 0.5 nm.

2.8. Horseradish peroxidase assay

The following test was performed to confirm the horseradish peroxidase (HRP)-like activity of bare and immobilized PB nanoparticles. This assay relies on the oxidation of guaiacol substrate by H_2O_2 in the presence of horseradish peroxidase or its mimic [36]. During the reaction, the color changes from colorless to a characteristic brown color, whose alteration was quantitatively analyzed by UV–Vis spectrophotometry. The guaiacol concentration was varied between 1 and 40 mM, while the concentrations of H_2O_2 and the enzymatic material were kept constant. The pH of the medium was set at 7.0 using phosphate buffer for the adjustment. Therefore, in each of the 2400 μL samples, a varied volume of 100 mM guaiacol stock solution was mixed with 240 μL of 100 ppm PB dispersion (or a dispersion that is 100 ppm in PB and 167 ppm in AL to obtain 600 mg/g dose), 912 μL of 131.6 mM phosphate buffer and a volume of ultrapure water to obtain a 2352 μL sample. The cuvette was then vortexed for 10 s. Finally, 48 μL of 135 mM H_2O_2 were added and the cuvette was immediately introduced into the spectrophotometer and the linear absorbance versus time plot was recorded at 470 nm. The slopes of absorbance versus time graphs represent the corresponding reaction rates (v) measured in absorbance unit per second. The reaction rate was converted to mM/s units by using the Beer-Lambert law. The optical light path is 1 cm and the molar extinction coefficient of the enzyme-catalyzed reaction product tetraguaiacol is 26.6 mM^{-1} cm^{-1}. Finally, the reaction rate was plotted as a function of the guaiacol concentration [S] in the corresponding sample. The horseradish peroxidase-like activity was assessed by fitting the plotted data with the Michaelis-Menten model of enzyme kinetics [37], as expressed in the following equation.

$$v = \frac{v_{max}}{K_m + [S]} \tag{3}$$

where v_{max} is the maximum possible rate regardless of the substrate concentration and K_m is the Michaelis-Menten constant.

2.9. Superoxide dismutase assay

To assess the ability of the nanozymes in dismutation of superoxide radical ions, the Fridovich assay was used [38], in which the radicals are generated by the oxidation of xanthine by xanthine oxidase. An indicator compound, nitroblue tetrazolium (NBT), helped to detect the antioxidant activity of the nanozyme of interest. The yellow colored NBT is reduced by the generated superoxide radical ions to form blue colored diformazan. In the presence of SOD or its mimicking materials, the generated radicals are totally or partially scavenged reducing the quantity of diformazan and thus, the intensity of blue color, which can be monitored spectrophotometrically.

In a typical measurement, a series of 3000 μL samples were prepared, in which only the nanozyme concentration was changed. The concentration of the PB was varied between 1 and 4 ppm. Further, the concentration of phosphate buffer in the samples was kept at 10 mM. In each sample, 200 μL of 3.0 mM xanthine and 100 μL of 3.0 mM NBT were mixed followed by volumes of PB stock as well as phosphate buffer to obtain 2700 μL sample. The cuvette was then vortexed for 10 s and 300 μL of 1.5 g/L xanthine oxidase was added to the sample. Immediately after the addition of xanthine oxidase, the cuvette was vortexed for 5 s and introduced into the spectrophotometer, the absorbance versus time values were recorded at 565 nm wavelength for 6 min. Furthermore, eight blanks were also measured, each of which was prepared by adding all reagents mentioned except the nanozyme and an additional volume of phosphate buffer were added to maintain a final volume of 3000 μL. The obtained data was interpreted by constructing the inhibition curve, a plot of the NBT reduction inhibition (I) as a function of nanozyme concentration in the sample. The inhibition can be calculated as follows.

$$I = \frac{\Delta A_o - \Delta A_s}{\Delta A_o} \cdot 100 \tag{4}$$

where ΔA_s is the change in absorbance during the 6 min measurement time for each sample and ΔA_o is the averaged value of 6 min absorbance change for the eight blank samples. The concentration of the nanozyme that causes a 50% inhibition is the so-called IC_{50} value.

Note that light scattering by the particles has a contribution to the absolute absorbance values during the assays, however, this factor was eliminated by using only the relative increase in the absorbances in the individual experiments.

3. Results and discussions

3.1. Characterization of the PB particles

The PB particles were prepared by the co-precipitation method [33] and the structure was confirmed by XPS and spectrophotometry. Concerning the latter technique, Fig. S1 shows the characteristic UV–Vis absorption spectrum of the obtained PB. The spectrum is characterized by a broad absorption band located at 700 nm, which is attributed to the charge transfer between Fe(II) and Fe(III) along Fe(II)–CN–Fe(III) confirming the successful synthesis of the desired PB.

The chemical composition of PB was explored with XPS. The survey scan reveals the presence of Fe, C, N, O and Au elements (Fig. 1), where the latter one is from the gold plated sample holder. The high-resolution deconvoluted XP spectra of Fe 2p, C 1s, N 1s and O 1s regions are shown in Fig. S2. The peaks at 708.69 eV and 710.29 eV in Fig. S2a are assigned to Fe(II) $2p_{3/2}$ and Fe(III) $2p_{3/2}$, respectively, which are in good accordance with literature values [39]. The presence of mixed-valence Fe indicates the formation of PB. The high resolution C 1s spectra was deconvoluted into four components, representing different chemical environments of the surface carbon moieties (Fig. S2b). The carbon in the ciano group of PB completely overlaps with the C-OH functionalities of the surface. Fig. S2c shows three majors peaks for the N 1s region, the peak at 397.78 eV is assigned to nitrogen in the cyanide ligands [39,40] while the one at 399.35 eV is attributed to charge transfer processes between surface moieties [41]. The peak at 402.3 eV indicates the presence of positively charged nitrogen, most likely ammonium ions, which has been observed for PB compounds in other reports as well [39]. A possible source of the ammonium ions is the mild heat treatment during the sample drying process. Another indirect indication of the presence of ammonium ions is seen in Fig. S2a. The Fe(II) satellite peak at 712.68 eV is indicative that the majority of the surface Fe(II) exists in a high-spin state. In classical PB, however, Fe(II) should exist solely in a low-spin state, as the cyanide ligand is a strong field ligand. Weak ligand field in the PB lattice is only experienced at the Fe(III) sites. The Fe(II) can occupy these sites in the presence of monovalent cations (such as NH_4^+), through the formation of an Everitt's salt type compounds (PB analogue) on the surface. The oxygen region in Fig. S2d can be fitted with one component centered at 532.76 eV, which corresponds to surface OH groups of the samples. The quantitative XPS composition analysis for all detected species resulted in the following composition (in atomic percentage, at.%) of the sample: 4.3% Fe, 53.1% C, 30.9% N and 11.7% O (Table S1).

The pH-dependence of PB particle size and charge was measured by DLS and electrophoresis, respectively (Fig. S3). The average hydrodynamic radius was found to be 42 nm at pH 4 and did not show any unambiguous trends by changing the pH. The electrophoretic mobility was determined to be $-1.5 \cdot 10^{-8}$ m^2/Vs and no clear pH-dependence was found in the pH regime 3–11. This mobility value corresponds to a zeta potential of around −19.7 mV, once the Smoluchowski model is used for the conversion [42]. The negative charge originates from the deprotonated surface hydroxyl and carboxyl groups leading to an electrostatic repulsion between the individual particles and subsequently, to hindered aggregation and stable particle stock dispersions under the storage conditions.

3.2. Homoaggregation of AL particles

To optimize the experimental conditions for aggregation rate measurements, the aggregation tendency of AL particles at different concentrations was studied via time resolved DLS. The background salt concentration, adjusted with KCl, was kept at 1.0 M KCl to ensure that all electrostatic repulsive interparticle forces are screened and thus, the particles undergo rapid aggregation, as suggested by the theory of Derjaguin, Landau, Verwey and Overbeek (DLVO) [43]. The results shown in Fig. S4 indicate that the slopes of the hydrodynamic radius versus time curves increase with the particle concentration. The apparent aggregation rate constants were calculated from these plots using Eq. (2). In addition, the half-time of aggregation ($T_{1/2}$), i.e., the time interval, under which half of the primary particles form dimers, was calculated using the following equation.

$$T_{1/2} = \frac{2}{kC_0} \tag{5}$$

where C_0 is the initial number concentration of the particles and k is the diffusion-controlled aggregation rate constant, as described by Smoluchowski [34]. The dependence of particle concentration on these values (Fig. S5) confirms that the apparent aggregation rate constant is larger in more concentrated dispersions and that the aggregation half-time decreases with the particle concentration. Based on these results, an AL concentration of 25 ppm was selected for further experiments. This value provides a good compromise as the early stage of the aggregation (i.e., no higher ranked aggregates form) can be followed, while the scattering intensity is high enough to perform reliable DLS measurements.

Using the selected experimental conditions above, the salt-induced aggregation of the AL particles was quantitatively assessed at different ionic strengths adjusted with KCl. The stability ratio value was calculated with Eq. (1) at each ionic strength value. The stability ratio significantly decreased as the KCl concentration was increased, until it reached unity indicating unstable dispersions and rapid particle aggregation (Fig. 2). Such a tendency is in line with the prediction by the DLVO theory. Accordingly, the background salt ions shrink the electric double layer around charged AL particles, therefore, the repulsive electrostatic forces weaken at higher salt concentrations. Until the threshold

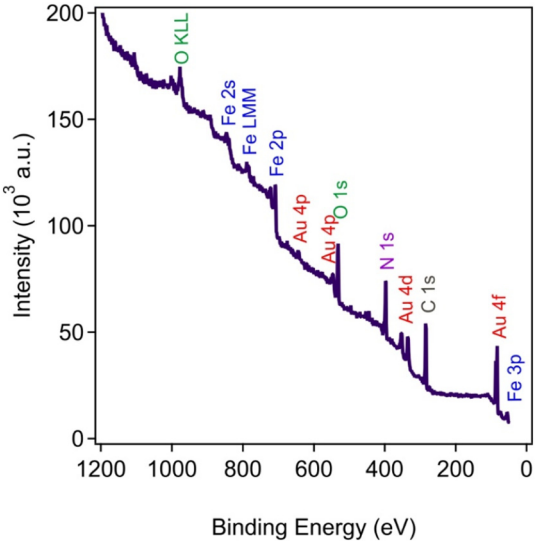

Fig. 1. XPS survey spectrum of the obtained PB nanoparticles in solid state. O KLL and Fe LMM are peaks of O and Fe for Auger transitions involving energy levels K, L and M.

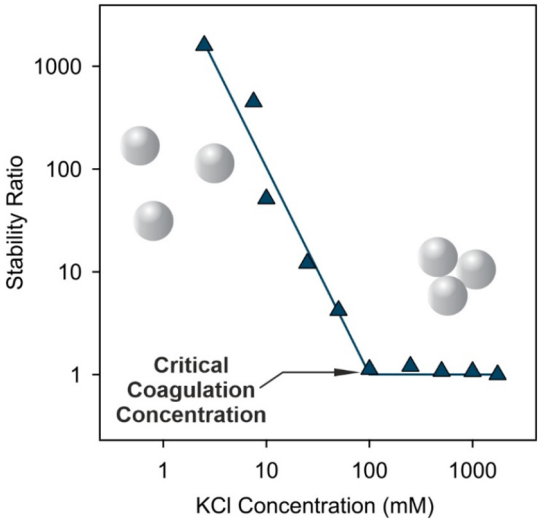

Fig. 2. Stability ratio values of 25 ppm AL dispersions as a function of the ionic strength adjusted by KCl at pH 4. The line serves to guide the eye.

concentration of 100 mM of KCl, so-called critical coagulation concentration, which separates slow and fast aggregation regimes, the double layer forces vanish and the particles undergo diffusion-controlled aggregation due to the predominance of the van der Waals attractive forces.

The ionic strength-dependent electrophoretic mobilities confirm the above explanation (Fig. 3). The values are positive at low salt levels due to the presence of the protonated amidine groups. As a result of the screening effect of the salt constituent ions on the surface charge, the mobilities decreased to almost zero by increasing the ionic strength. This clearly indicates the weakening of the electrostatic double layer repulsion, which is proportional to the charge of the particles [43]. Similar aggregation and charging properties were reported for latex particles in the presence of simple salts [34,44,45].

3.3. Heteroaggregation of AL and PB particles

Decoration of AL particles with oppositely charged PB nanoparticles occurred as a result of their controlled heteroaggregation. Their sizes are significantly different, the hydrodynamic radii were determined to be 249 nm for AL and 42 nm for PB (Table 1 and Fig. S6) in stable dispersions. This difference is also demonstrated by TEM images shown in Fig. S7. The DLS measurements carried out in stable dispersions indicated monomodal particle size distribution with good and moderate polydispersity for AL and PB, respectively. The scattered intensity of AL was higher at the same mass concentrations indicating that the AL particles scatters light much more and thus, they can be primarily detected by light scattering techniques, once both AL and PB particles are dispersed in the same sample. The magnitude of the electrophoretic mobility measured in stable dispersions was much higher for AL than for PB particles (Table 1). In the heteroaggregation experiments, i.e., particle collisions between AL and PB, the AL concentration was kept constant (25 ppm selected in the previous section), while the PB dose was systematically varied.

The charging properties were assessed with electrophoresis (Fig. 4). The electrophoretic mobilities gradually decreased as the PB dose increased with a characteristic range, where electrophoretic mobility values changed from positive to negative. At low PB doses, the electrophoretic mobilities are positive indicating an overall positive charge of the composites owing to the limited amount of adsorbed PB particles. As the PB dose increased, more negatively charged PB accumulated on the surface of the positively charged AL. When the amount of positive and negative charges was balanced, the AL-PB particles showed net zero charge, called isoelectric point (IEP). Further additions of PB generated AL-PB composites of an overall negative charge. Such a charge reversal was reported earlier for oppositely charged particle-polyelectrolyte systems [45–50] and also for latexes in the presence of clays [51,52]. The mobilities reached saturation at high PB doses, where the AL surface became saturated with adsorbed PB nanoparticles at the onset of the mobility plateau.

Table 1
Characteristic size and charge parameters for AL and PB particles determined in stable dispersions at 25 ppm concentrations, 1 mM ionic strength and pH 4.

Material	R_h[a] (nm)	I_s[a] (kcps)[a]	PDI[a] (%)	EM[a] (10^{-8} m^2/Vs)
AL	249	305	13.4	3.2
PB	42	168	23.5	−1.5

[a] R_h is the hydrodynamic radius, I_s is the scattering intensity, PDI is the polydispersity index, EM is the electrophoretic mobility and the unit kcps stands for to kilo counts per second.

To assess the colloidal stability of the above dispersions, the stability ratios were measured under the same experimental conditions (Fig. 5). It is evident from the data that the gradual decrease in mobility values affected the stability of the AL-PB dispersions. Accordingly, at larger magnitude of the electrophoretic mobility values (both in the positive and negative regimes corresponding to low and high PB doses, respectively), the stability ratio values are large indicating rather stable dispersions. However, in the regions surrounding the IEP, the stability ratios drop to a value of one, which refers to rapid particle aggregation and to unstable dispersions. One significant observation, which is worthy of further discussion, is the presence of plateaus in the stability ratio values at low and high doses. The same trends were reported for polyelectrolyte-coated particles [53], which clearly indicate a similar origin of the interparticle forces for the bare and the PB-covered AL particles. Several studies have been reported for latex particle dispersions, in which the predominating interparticle forces were assigned to DLVO-type interaction [44,45,47], as discussed earlier in the previous section. Therefore, it is certain that the PB coating does not lead to the raise of additional interaction forces and the aggregation mechanism is driven by the balance between DLVO-type electrostatic double layer repulsion and van der Waals attraction. The latter one predominates around the IEP, where the overall charge of the AL-PB particles is zero and hence, the double layer forces vanish. Note that the agreement between the measured tendency in the stability ratios with the DLVO theory is purely

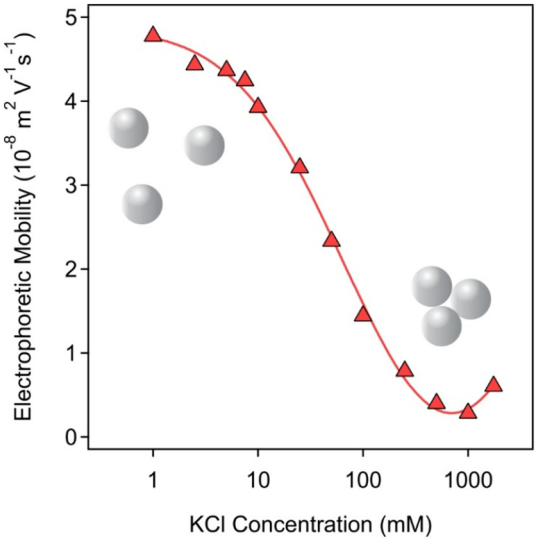

Fig. 3. Electrophoretic mobilities of 25 ppm AL dispersions as a function of ionic strength adjusted with KCl at pH 4. The lines serve to guide the eyes.

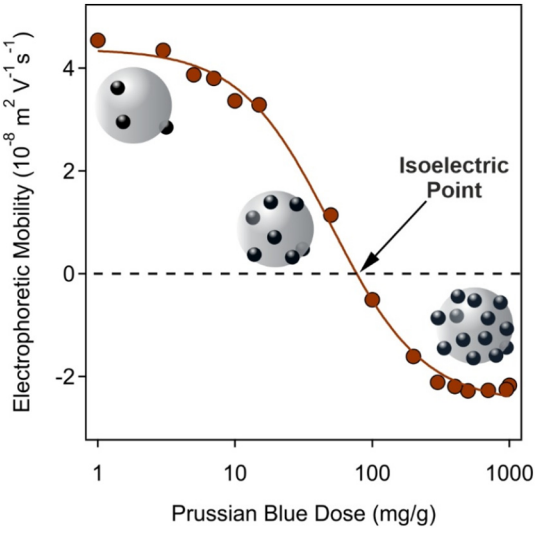

Fig. 4. Electrophoretic mobilities of AL particles at various PB concentrations at 1 mM ionic strength. The concentration of PB is expressed as dose, measured in mg/g (mg PB per one gram of AL). The lines serve to guide the eyes.

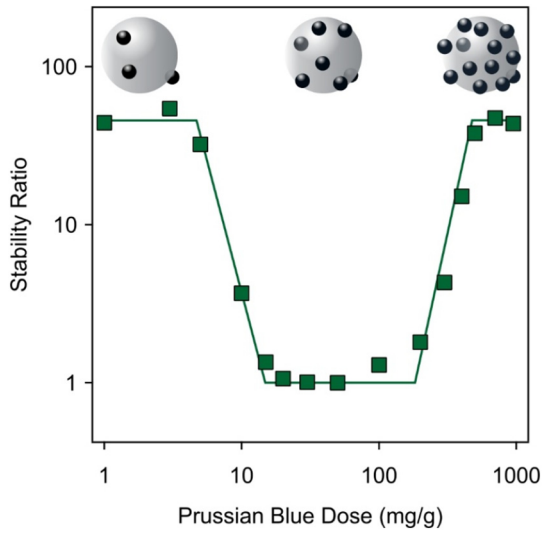

Fig. 5. Stability ratio values of AL-PB dispersions with different concentrations of PB. The concentration of PB is expressed as doses, measured in mg/g (mg PB per one gram of AL). The concentration of AL was kept at 25 ppm, while the ionic strength was 1 mM and the pH is 4. The solid line is to guide the eyes.

qualitative, since the extent of the interparticle forces cannot be calculated from the present results.

The coating process was also visualized by TEM/SEM images recorded at PB doses of 1, 30, and 600 mg/g (Fig. 6). In general, the particles were slightly agglomerated owing to the drying process during sample preparation. However, the images clearly show that more PB nanoparticles were immobilized as the dose increases. At the lowest dose, only a few PB nanoparticles could be detected on the AL surface, while at 30 mg/g, the AL particles are partially covered. The charge neutralization occurred around this dose, as pointed out in the electrophoretic mobility studies earlier. Finally, at 600 mg/g, the PB nanoparticles were uniformly distributed on the surface of AL. Note that the dispersions were found to be stable under the latter experimental condition. This dose was used later to assess the antioxidant activity of the hybrid AL-PB composite, denoted as AL-PB-600 in the following sections.

3.4. Antioxidant activity

The HRP-like function of the PB and AL-PB-600 particles was assessed via the guaiacol assay, in which, guaiacol is oxidized by H_2O_2 in the presence of the catalysts [36]. The obtained reaction rate data were plotted as a function of the substrate concentration (Fig. 7) and they fitted well to theoretical values determined by the Michaelis-Menten theory (Eq. (3)). The obtained v_{max} as well as K_m values are shown in Table 2. The v_{max} is the maximum reaction rate observed, where further increase in the substrate concentration does not increase the rate any further due to saturation of the catalytic sites of the enzyme or its mimics. The K_m is the guaiacol concentration that correspond to the rate half that of the v_{max}. The K_m value is a measure of the affinity between the enzyme or its mimics and the substrate, the lower the K_m, the higher the affinity between the enzymatic material and the substrate.

The obtained parameters for PB and AL-PB-600 were in the same range, i.e., the immobilization of the PB particles did not affect their HRP-like activity significantly. Similar values were reported also for the native enzyme [54], however, straight comparison is difficult due to the variation in added amount and the different chemical structure of the catalysts.

The ability of the PB and AL-PB-600 materials in dismutation of superoxide radical ions was tested by the Fridovich assay [38]. The inhibition of the NBT-radical reaction was calculated using Eq. (4) and presented as a function of the PB concentration in Fig. 8. A number of conclusions can be drawn based on the data. The PB did not lose the SOD activity upon immobilization on AL. However, because of inevitable hindrance of some catalytic sites on the surfaces of PB particles upon attachment to the AL latex surface, the maximum inhibition values decreased for AL-PB-600. Nevertheless, The IC_{50} values for PB and AL-PB-600 were very similar (Table 2), but significantly higher than the IC_{50} for native SOD. Because of the large difference in the nature of the materials, the direct comparison of the data is difficult. The retainment of SOD activity for AL-PB-600 is very promising in applications, where bare PB nanoparticles are likely to form an unstable colloid.

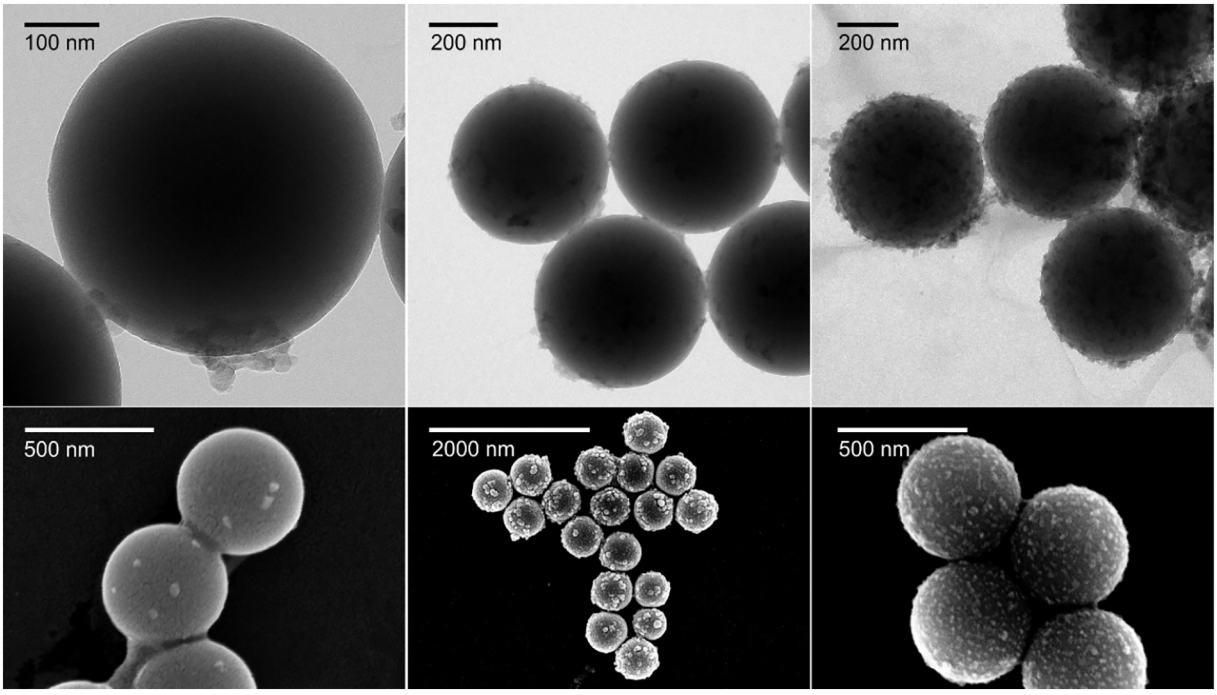

Fig. 6. Dried state TEM (upper row) and SEM (lower row) images of AL-PB systems at PB dose of 1 mg/g (left), 30 mg/g (middle) and 600 mg/g (right).

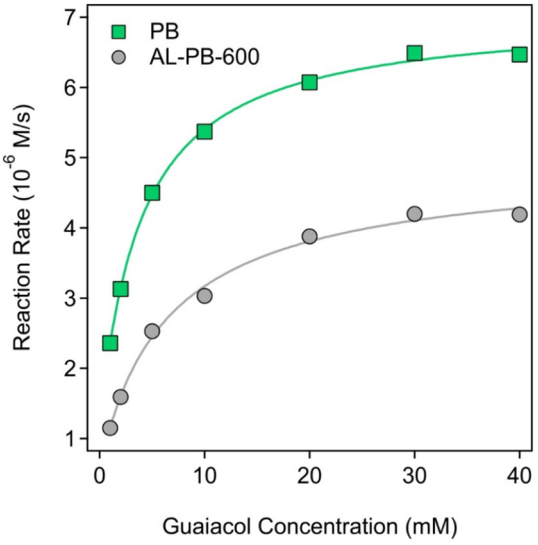

Fig. 7. HRP activity of PB (green squares) and AL-PB-600 (grey circles) particles. The solid lines are the Michaelis-Menten fits described by Eq. (3).

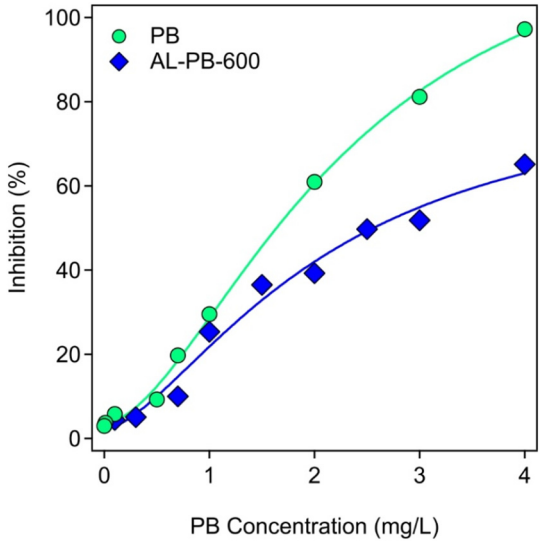

Fig. 8. Inhibition of the NBT-superoxide radical ion reaction by the PB (green circles) and AL-PB-600 (blue diamonds) particles. The inhibition values were obtained using Eq. (4). The solid lines are just to guide the eyes.

Note that the pH was different during the preparation of the AL-PB-600 (pH 4) and in the above assays (pH 7). However, neither AL nor PB particles change the sign of charge (positive and negative, respectively) during such a shift in the pH and thus, the AL-PB-600 structure remained stable in the enzymatic test reactions too.

4. Conclusions

PB nanoparticles of antioxidant activity were synthesized and formulated by heteroaggregation with AL particles. This heteroaggregation can be also rationalized as an adsorption process of the PB nanoparticles on the AL surface due to their opposite charges. The structure of the bare PB was confirmed with UV–Vis spectrophotometry and XPS measurements, while the characteristic size and charge values of both particles were studied by electrophoretic and dynamic light scattering. The PB nanoparticles adsorbed strongly on the AL surface leading to charge neutralization and charge reversal at appropriate PB doses. The colloidal stability of the samples was assessed and confirmed that the aggregation of the PB-decorated AL particles is driven by DLVO-type forces. Accordingly, the electrostatic double layer repulsion stabilizes the dispersions at low and high PB doses, where the PB functionalized particles possess significant charge. At the IEP, however, the particles undergo diffusion-controlled aggregation due to the lack of charges, i.e., to the disappearance of the electrostatic double layers and predominance of attractive van der Waals forces. To test the antioxidant activity of the AL-PB composite, a PB dose of 600 mg/g, at which the overall charge was negative and a stable colloid is formed, was selected. The AL-PB-600 particles showed good antioxidant properties in two assays. Accordingly, HRP-like activity of PB was maintained upon immobilization on AL and the calculated Michaelis-Menten parameters were in good agreement for PB and AL-PB-600. The results of the SOD-like activity study indicated that blocking the active sites of PB upon immobilization onto the AL surface led to a decrease in the ability to dismutate superoxide radical ions, however, the IC_{50} values were still in the range, where the AL-PB-600 hybrid can be considered as an efficient SOD mimic. These facts indicate that the obtained AL-PB-600 composites can be effectively used for superoxide radical ion dismutation as well as for H_2O_2 consumption in heterogeneous systems, wherever the aim is to reduce the concentration of ROS.

Table 2
Comparison of the results of HRP and SOD activity assays obtained for the PB, AL-PB-600 and native enzymes.

Material	K_m (mM)[a]	v_{max} (10^{-6} M/s)[a]	IC_{50} (mg/L)[b]
PB	2.19[c]	6.71[c]	1.64
AL-PB-600	2.92[c]	4.09[c]	2.55
Native enzyme	3.23[d]	2.80[d]	0.07[e]

[a] Calculated from the HRP assay data by Eq. (3) with an error of 1%.
[b] Determined in SOD activity assays with an average error of 5%.
[c] A PB concentration of 10 ppm was applied in the assays.
[d] The value is taken from Reference [54].
[e] Reference [55].

CRediT authorship contribution statement

Nizar B. Alsharif: Investigation, Writing - original draft, Visualization. **Gergely F. Samu:** Investigation, Writing - original draft, Visualization. **Szilárd Sáringer:** Methodology, Software, Writing - review & editing. **Szabolcs Muráth:** Validation, Investigation, Writing - review & editing. **Istvan Szilagyi:** Conceptualization, Writing - original draft, Supervision, Funding acquisition, Writing - review & editing.

Declaration of competing interest

The authors declare that they have no known competing financial interests or personal relationships that could have appeared to influence the work reported in this paper.

Acknowledgments

This research was financially supported by the Lendület program of the Hungarian Academy of Sciences (96130) and by the Ministry of Human Capacities, Hungary (20391-3/2018/FEKUSTRAT). The authors are also thankful for the support of the University of Szeged Open Access Fund (4698).

Appendix A. Supplementary data

Supplementary data to this article can be found online at https://doi.org/10.1016/j.molliq.2020.113066.

References

[1] S.J. Benkovic, S. Hammes-Schiffer, A perspective on enzyme catalysis, Science 301 (5637) (2003) 1196–1202.

[2] X. Ma, A.C. Hortelao, T. Patino, S. Sanchez, Enzyme catalysis to power micro/nanomachines, ACS Nano 10 (10) (2016) 9111–9122.
[3] H. Wei, E.K. Wang, Nanomaterials with enzyme-like characteristics (nanozymes): next-generation artificial enzymes, Chem. Soc. Rev. 42 (14) (2013) 6060–6093.
[4] L. Qin, X.Y. Wang, Y.F. Liu, H. Wei, 2D-metal-organic-framework-nanozyme sensor arrays for probing phosphates and their enzymatic hydrolysis, Anal. Chem. 90 (16) (2018) 9983–9989.
[5] F. Chen, M. Bai, K. Cao, Y. Zhao, J. Wei, Y.X. Zhao, Fabricating MnO_2 nanozymes as intracellular catalytic DNA circuit generators for versatile imaging of base-excision repair in living cells, Adv. Funct. Mater. 27 (45) (2017)1702748.
[6] Y.H. Lin, J.S. Ren, X.G. Qu, Catalytically active nanomaterials: a promising candidate for artificial enzymes, Accounts Chem. Res. 47 (4) (2014) 1097–1105.
[7] L. Valgimigli, A. Baschieri, R. Amorati, Antioxidant activity of nanomaterials, J. Mat. Chem. B 6 (14) (2018) 2036–2051.
[8] C.C. Winterbourn, Reconciling the chemistry and biology of reactive oxygen species, Nat. Chem. Biol. 4 (5) (2008) 278–286.
[9] P. Brenneisen, A.S. Reichert, Nanotherapy and reactive oxygen species (ROS) in cancer: a novel perspective, Antioxidants 7 (2) (2018) 31.
[10] C. Nirmala, M.S. Bisht, H.K. Bajwa, O. Santosh, Bamboo: a rich source of natural antioxidants and its applications in the food and pharmaceutical industry, Trends Food Sci. Technol. 77 (2018) 91–99.
[11] J.W. Finley, A.N. Kong, K.J. Hintze, E.H. Jeffery, L.L. Ji, X.G. Lei, Antioxidants in foods: state of the science important to the food industry, J. Agric. Food Chem. 59 (13) (2011) 6837–6846.
[12] A.A. Vernekar, D. Sinha, S. Srivastava, P.U. Paramasivam, P. D'Silva, G. Mugesh, An antioxidant nanozyme that uncovers the cytoprotective potential of vanadia nanowires, Nat. Commun. 5 (2014) 5301.
[13] F. Dashtestani, H. Ghourchian, A. Najafi, Albumin coated copper-cysteine nanozyme for reducing oxidative stress induced during sperm cryopreservation, Bioorg. Chem. 80 (2018) 621–630.
[14] F.M. Wang, E.G. Ju, Y.J. Guan, J.S. Ren, X.G. Qu, Light-mediated reversible modulation of ROS level in living cells by using an activity-controllable nanozyme, Small 13 (25) (2017) 1603051.
[15] M. Moglianetti, E. De Luca, P.A. Deborah, R. Marotta, T. Catelani, B. Sartori, H. Amenitsch, S.F. Retta, P.P. Pompa, Platinum nanozymes recover cellular ROS homeostasis in an oxidative stress-mediated disease model, Nanoscale 8 (6) (2016) 3739–3752.
[16] T.M. Chen, H. Zou, X.J. Wu, C.C. Liu, B. Situ, L. Zheng, G.W. Yang, Nanozymatic antioxidant system based on MoS_2 nanosheets, ACS Appl. Mater. Interfaces 10 (15) (2018) 12453–12462.
[17] N. Singh, M.A. Savanur, S. Srivastava, P. D'Silva, G. Mugesh, A redox modulatory Mn_3O_4 nanozyme with multi-enzyme activity provides efficient cytoprotection to human cells in a Parkinson's disease model, Angew. Chem.-Int. Edit. 56 (45) (2017) 14267–14271.
[18] A. Pratsinis, G.A. Kelesidis, S. Zuercher, F. Krumeich, S. Bolisetty, R. Mezzenga, J.C. Leroux, G.A. Sotiriou, Enzyme-mimetic antioxidant luminescent nanoparticles for highly sensitive hydrogen peroxide biosensing, ACS Nano 11 (12) (2017) 12210–12218.
[19] Y.Y. Huang, C.Q. Liu, F. Pu, Z. Liu, J.S. Ren, X.G. Qu, A GO-Se nanocomposite as an antioxidant nanozyme for cytoprotection, Chem. Commun. 53 (21) (2017) 3082–3085.
[20] W. Zhang, S.L. Hu, J.J. Yin, W.W. He, W. Lu, M. Ma, N. Gu, Y. Zhang, Prussian blue nanoparticles as multienzyme mimetics and reactive oxygen species scavengers, J. Am. Chem. Soc. 138 (18) (2016) 5860–5865.
[21] Y.Y. Huang, Z. Liu, C.Q. Liu, E.G. Ju, Y. Zhang, J.S. Ren, X.G. Qu, Self-assembly of multinanozymes to mimic an intracellular antioxidant defense system, Angew. Chem.-Int. Edit. 55 (23) (2016) 6646–6650.
[22] M.K. Masud, J. Na, M. Younus, M.S.A. Hossain, Y. Bando, M.J.A. Shiddiky, Y. Yamauchi, Superparamagnetic nanoarchitectures for disease-specific biomarker detection, Chem. Soc. Rev. 48 (24) (2019) 5717–5751.
[23] M.S. Moorthy, G. Hoang, B. Subramanian, N.Q. Bui, M. Panchanathan, S. Mondal, V.P.T. Tuong, H. Kim, J. Oh, Prussian blue decorated mesoporous silica hybrid nanocarriers for photoacoustic imaging-guided synergistic chemo-photothermal combination therapy, J. Mat. Chem. B 6 (32) (2018) 5220–5233.
[24] G.W. Bishop, J.E. Satterwhite, S. Bhakta, K. Kadimisetty, K.M. Gillette, E. Chen, J.F. Rusling, 3D-printed fluidic devices for nanoparticle preparation and flow-injection amperometry using integrated Prussian blue nanoparticle-modified electrodes, Anal. Chem. 87 (10) (2015) 5437–5443.
[25] Y. Chen, L. Wu, Q. Wang, M. Wu, B. Xu, X. Liu, J. Liu, Toxicological evaluation of Prussian blue nanoparticles after short exposure of mice, Hum. Exp. Toxicol. 35 (10) (2016) 1123–1132.
[26] M. Shokouhimehr, E.S. Soehnlen, J.H. Hao, M. Griswold, C. Flask, X.D. Fan, J.P. Basilion, S. Basu, S.P.D. Huang, Dual purpose Prussian blue nanoparticles for cellular imaging and drug delivery: a new generation of T-1-weighted MRI contrast and small molecule delivery agents, J. Mater. Chem. 20 (25) (2010) 5251–5259.
[27] H. Oh, J.S. Lee, D. Sung, J.H. Lee, S.H. Moh, J.M. Lim, W.I. Choi, Synergistic antioxidant activity of size controllable chitosan-templated Prussian blue nanoparticle, Nanomedicine 14 (19) (2019) 2567–2578.
[28] X.Q. Zhang, S.W. Gong, Y. Zhang, T. Yang, C.Y. Wang, N. Gu, Prussian blue modified iron oxide magnetic nanoparticles and their high peroxidase-like activity, J. Mater. Chem. 20 (24) (2010) 5110–5116.
[29] L. Cheng, H. Gong, W.W. Zhu, J.J. Liu, X.Y. Wang, G. Liu, Z. Liu, PEGylated Prussian blue nanocubes as a theranostic agent for simultaneous cancer imaging and photothermal therapy, Biomaterials 35 (37) (2014) 9844–9852.
[30] W. Zhao, J.J. Xu, C.G. Shi, H.Y. Chen, Multilayer membranes via layer-by-layer deposition of organic polymer protected Prussian blue nanoparticles and glucose oxidase for glucose biosensing, Langmuir 21 (21) (2005) 9630–9634.
[31] X.D. Li, X.L. Liang, F. Ma, L.J. Jing, L. Lin, Y.B. Yang, S.S. Feng, G.L. Fu, X.L. Yue, Z.F. Dai, Chitosan stabilized Prussian blue nanoparticles for photothermally enhanced gene delivery, Colloid Surf. B-Biointerfaces 123 (2014) 629–638.
[32] T. Uemura, S. Kitagawa, Prussian blue nanoparticles protected by poly (vinylpyrrolidone), J. Am. Chem. Soc. 125 (26) (2003) 7814–7815.
[33] W.M. Zhang, D. Ma, J.X. Du, Prussian blue nanoparticles as peroxidase mimetics for sensitive colorimetric detection of hydrogen peroxide and glucose, Talanta 120 (2014) 362–367.
[34] H. Holthoff, S.U. Egelhaaf, M. Borkovec, P. Schurtenberger, H. Sticher, Coagulation rate measurements of colloidal particles by simultaneous static and dynamic light scattering, Langmuir 12 (23) (1996) 5541–5549.
[35] F. Iselau, T.P. Xuan, G. Trefalt, A. Matic, K. Holmberg, R. Bordes, Formation and relaxation kinetics of starch-particle complexes, Soft Matter 12 (47) (2016) 9509–9519.
[36] A.C. Maehly, B. Chance, The assay of catalases and peroxidases, Methods Biochem. Anal. 1 (1954) 357–424.
[37] K.A. Johnson, R.S. Goody, The original Michaelis constant: translation of the 1913 Michaelis-Menten paper, Biochemistry 50 (39) (2011) 8264–8269.
[38] C. Beaucham, I. Fridovich, Superoxide dismutase - improved assays and an assay applicable to acrylamide gels, Anal. Biochem. 44 (1) (1971) 276–287.
[39] X.W. He, L.D. Tian, M.T. Qiao, J.Z. Zhang, W.C. Geng, Q.Y. Zhang, A novel highly crystalline Fe-4(Fe(CN)(6))(3) concave cube anode material for Li-ion batteries with high capacity and long life, J. Mater. Chem. A 7 (18) (2019) 11478–11486.
[40] A. Forment-Aliaga, R.T. Weitz, A.S. Sagar, E.J.H. Lee, M. Konuma, M. Burghard, K. Kern, Strong p-type doping of individual carbon nanotubes by Prussian blue functionalization, Small 4 (10) (2008) 1671–1675.
[41] E. Fluck, H. Inoue, S. Yanagisawa, Mossbauer and X-ray photoelectron spectroscopic studied of Prussian blue and its related compounds, Z. Anorg. Allg. Chem. 430 (3) (1977) 241–249.
[42] A.V. Delgado, E. Gonzalez-Caballero, R.J. Hunter, L.K. Koopal, J. Lyklema, Measurement and interpretation of electrokinetic phenomena - (IUPAC technical report), Pure Appl. Chem. 77 (10) (2005) 1753–1805.
[43] G. Trefalt, I. Szilagyi, M. Borkovec, Poisson-Boltzmann description of interaction forces and aggregation rates involving charged colloidal particles in asymmetric electrolytes, J. Colloid Interface Sci. 406 (2013) 111–120.
[44] F.J.M. Ruiz-Cabello, G. Trefalt, T. Oncsik, I. Szilagyi, P. Maroni, M. Borkovec, Interaction forces and aggregation rates of colloidal latex particles in the presence of monovalent counterions, J. Phys. Chem. B 119 (25) (2015) 8184–8193.
[45] S. Saringer, R.A. Akula, A. Szerlauth, I. Szilagyi, Papain adsorption on latex particles: charging, aggregation, and enzymatic activity, J. Phys. Chem. B 123 (46) (2019) 9984–9991.
[46] G. Gillies, W. Lin, M. Borkovec, Charging and aggregation of positively charged latex particles in the presence of anionic polyelectrolytes, J. Phys. Chem. B 111 (29) (2007) 8626–8633.
[47] I. Szilagyi, G. Trefalt, A. Tiraferri, P. Maroni, M. Borkovec, Polyelectrolyte adsorption, interparticle forces, and colloidal aggregation, Soft Matter 10 (15) (2014) 2479–2502.
[48] I. Popa, G. Papastavrou, M. Borkovec, Charge regulation effects on electrostatic patch-charge attraction induced by adsorbed dendrimers, Phys. Chem. Chem. Phys. 12 (2010) 4863–4871.
[49] L. Avadiar, Y.K. Leong, Interactions of PEI (polyethylenimine)-silica particles with citric acid in dispersions, Colloid Polym. Sci. 289 (3) (2011) 237–245.
[50] T.D. Chaparro, R.D. Silva, I.S. Monteiro, A. Barros-Timmons, R. Giudici, A.M. dos Santos, E. Bourgeat-Lami, Interaction of cationic, anionic, and nonionic macroraft homo- and copolymers with laponite clay, Langmuir 35 (35) (2019) 11512–11523.
[51] M. Pavlovic, P. Rouster, E. Bourgeat-Lami, V. Prevot, I. Szilagyi, Design of latex-layered double hydroxide composites by tuning the aggregation in suspensions, Soft Matter 13 (4) (2017) 842–851.
[52] M. Kobayashi, M. Nitanai, N. Satta, Y. Adachi, Coagulation and charging of latex particles in the presence of imogolite, Colloid Surf. A 435 (2013) 139–146.
[53] J. Hierrezuelo, A. Sadeghpour, I. Szilagyi, A. Vaccaro, M. Borkovec, Electrostatic stabilization of charged colloidal particles with adsorbed polyelectrolytes of opposite charge, Langmuir 26 (19) (2010) 15109–15111.
[54] M. Pavlovic, P. Rouster, Z. Somosi, I. Szilagyi, Horseradish peroxidase-nanoclay hybrid particles of high functional and colloidal stability, J. Colloid Interface Sci. 524 (2018) 114–121.
[55] M. Pavlovic, P. Rouster, I. Szilagyi, Synthesis and formulation of functional bionanomaterials with superoxide dismutase activity, Nanoscale 9 (1) (2017) 369–379.